Science of Remote Sensing 4 (2021) 100036

Contents lists available at ScienceDirect

Science of Remote Sensing

journal homepage: www.sciencedirect.com/journal/science-of-remote-sensing

The Arctic Nearshore Turbidity Algorithm (ANTA) - A multi sensor turbidity algorithm for Arctic nearshore environments

Konstantin P. Klein [a,b,*], Hugues Lantuit [a,b], Birgit Heim [b], David Doxaran [c], Bennet Juhls [b], Ingmar Nitze [b], Daniela Walch [b,d], Amanda Poste [e,f], Janne E. Søreide [d]

[a] Institute of Geosciences, University of Potsdam, Potsdam, Germany
[b] Permafrost Research Section, Alfred Wegener Institute Helmholtz Centre for Polar and Marine Science, Potsdam, Germany
[c] Laboratoire d'Océanographie de Villefranche, UMR 7093 CNRS-SU, 06230, Villefranche-sur-Mer, France
[d] Department of Arctic Biology, The University Centre in Svalbard (UNIS), Longyearbyen, Norway
[e] Norwegian Institute for Water Research (NIVA), Tromsø, Norway
[f] Department of Arctic and Marine Biology, UiT–The Arctic University of Norway, Tromsø, Norway

ARTICLE INFO

Keywords:
Ocean color remote sensing
Turbidity retrieval
Nearshore zone
Arctic Ocean

ABSTRACT

The Arctic is greatly impacted by climate change. The increase in air temperature drives the thawing of permafrost and an increase in coastal erosion and river discharge. This leads to a greater input of sediment and organic matter into coastal waters, which substantially impacts the ecosystems by reducing light transmission through the water column and altering the biogeochemistry, but also the subsistence economy of local people, and changes in climate because of the transformation of organic matter into greenhouse gases. Yet, the quantification of suspended sediment in Arctic coastal and nearshore waters remains unsatisfactory due to the absence of dedicated algorithms to resolve the high loads occurring in the close vicinity of the shoreline. In this study we present the Arctic Nearshore Turbidity Algorithm (ANTA), the first reflectance-turbidity relationship specifically targeted towards Arctic nearshore waters that is tuned with in-situ measurements from the nearshore waters of Herschel Island Qikiqtaruk in the western Canadian Arctic. A semi-empirical model was calibrated for several relevant sensors in ocean color remote sensing, including MODIS, Sentinel 3 (OLCI), Landsat 8 (OLI), and Sentinel 2 (MSI), as well as the older Landsat sensors TM and ETM+. The ANTA performed better with Landsat 8 than with Sentinel 2 and Sentinel 3. The application of the ANTA to Sentinel 2 imagery that matches in-situ turbidity samples taken in Adventfjorden, Svalbard, shows transferability to nearshore areas beyond Herschel Island Qikiqtaruk.

1. Introduction

Climate change is stronger in the Arctic than anywhere else on Earth (Serreze and Barry, 2011): intensified permafrost thaw (Biskaborn et al., 2019), increased river discharge (McClelland et al., 2016) and stronger coastal erosion (Fritz et al., 2017) have significant impacts on the biophysical system. Permafrost coasts are particularly vulnerable to warming air temperatures, as frozen sediments thaw and become vulnerable to wave erosion (Lantuit and Pollard, 2008; McGillivray et al., 1993). Recent studies have shown that this has the potential to mobilize large carbon pools stored in permafrost (Tank et al., 2018), to release carbon and nutrients into nearshore areas (Fritz et al., 2017), or to release greenhouse gases directly into the atmosphere (Romanovsky et al., 2010; Tanski et al., 2019; Vonk et al., 2012).

Arctic nearshore and shelf areas have experienced increased sediment input due to increased river discharge, increased coastal erosion and increased glacial melting during the last decades (Déry et al., 2009; Jones et al., 2009; McClelland et al., 2006; World Glacier Monitoring Service, 2020). Arctic coasts are eroding at a mean annual rate of 0.5 m/a (Lantuit et al., 2013), leading to enhanced sediment input to nearshore areas. These sediments are likely to contain large amounts of carbon given the high organic matter content of coastal permafrost (Fritz et al., 2017). While the riverine influx of sediments to the Arctic Ocean has been quantified using *in-situ* and remote sensing data in several studies (Holmes et al., 2002), the sediment fluxes associated with coastal erosion are not well known. Recent research suggested that

* Corresponding author. Institute of Geosciences, University of Potsdam, Potsdam, Germany.
E-mail address: konstantin.klein@awi.de (K.P. Klein).

https://doi.org/10.1016/j.srs.2021.100036
Received 29 September 2021; Received in revised form 12 November 2021; Accepted 13 November 2021
Available online 15 November 2021

coastal erosion can be the main sediment contributor to Arctic nearshore areas outside large river deltas (Klein et al., 2019; Terhaar et al., 2021; Wegner et al., 2015).

Nearshore areas, defined as sea water shallower than 20 m along the coast (Fritz et al., 2017), remain understudied in Arctic Oceanography. This is mostly due to the traditional division of disciplines between terrestrial and marine science and the logistical challenges associated with measurements in shallow waters close to the shoreline. Yet, these areas play a crucial role in the carbon cycle: coastal erosion and resuspension cause a steady supply of carbon-rich material in surface waters, where they could be transformed to and released as greenhouse gases (Jong et al., 2020). Recent research indicated that Carbon burial in nearshore waters is rare due to constant wave induced resuspension (Jong et al., 2020). Little research has been conducted on the effects of coastal erosion on turbidity in Arctic coastal waters. Increases in turbidity are likely to impact primary production through reduced solar light penetration in the water column (Carmack and Wassmann, 2006), which could impact local food webs and eventually the subsistence economy of local people (Dunton et al., 2006).

Remote sensing has the potential to provide important insight into Arctic surface water geochemistry since it overcomes the problem of difficult accessibility of most field sites and is capable of covering large regions at a high frequency. Recent studies have shown the capability of ocean color remote sensing to study coastal waters (Groom et al., 2019), however, most studies focus on large river deltas (Constantin et al., 2017; Manzo et al., 2018) or use low spatial resolution imagery exclusively (Doxaran et al., 2012; Tang et al., 2013). Nearshore sediment flux analyses are less common, particularly in the Arctic.

Recent improvements in satellite borne optical instruments such as OLI onboard Landsat 8 and MSI onboard Sentinel 2 (Vanhellemont and Ruddick, 2014) and progress in atmospheric correction algorithms (Pahlevan et al., 2021; Vanhellemont and Ruddick, 2018, 2021) have opened new opportunities to resolve nearshore water characteristics at high spectral and spatial resolution. Nearshore waters are optically complex, as they are influenced by colored dissolved organic matter (cDOM), phytoplankton pigments, and suspended sediments, which makes remote sensing applications more error-prone.

Turbidity caused by suspended sediments is generally well correlated to the reflectance in the red to near-infrared (NIR) part of the electromagnetic spectrum (Munday and Alföldi, 1979), with the reflectance in the red part of the spectrum being more sensitive to low to intermediate turbidity values and the NIR reflectance being more sensitive to high turbidity values. Satellite based turbidity retrieval improved drastically with the introduction of semi-empirical relationships (Nechad et al., 2009). The most widely used semi-empirical turbidity algorithm was published by Dogliotti et al. (2015), where both red and NIR reflectances are used to cover a wide range of turbidity values. Validation data from multiple coastal sites located in the temperate to tropical parts of the Earth were used, with a strong focus on estuarine environments. Validation data from permafrost coasts is missing in this algorithm, even though permafrost coasts represent one third of the world's coastlines (Lantuit et al., 2013).

In this study, we calibrate and test the Arctic Nearshore Turbidity Algorithm (ANTA), an ocean color algorithm that directly relates water leaving reflectance to turbidity in Arctic surface nearshore waters. The goal of this study is to establish a robust turbidity-reflectance relationship which can adequately represent the complex nature of Arctic nearshore environments. In-situ measurements of water leaving reflectance, turbidity, and suspended particulate matter (SPM) concentration were used to calibrate an algorithm for multiple satellite sensors that are currently used for nearshore turbidity retrieving (Landsat 8, Sentinel 2, and Sentinel 3). Match-up scenes of Sentinel 2 with in-situ samples from a separate test area were used to test the performance of the ANTA. This algorithm should serve as a multi-sensor turbidity algorithm that is specifically calibrated for an Arctic nearshore environment with the high potential to transfer it to other Arctic coastal waters for larger-scale applications.

2. Methods

2.1. Regional setting

The tuning of the ANTA is based on in-situ measurements from the nearshore waters around Herschel Island Qikiqtaruk (HIQ), located at the Yukon coast in the western Canadian Arctic. *In-situ* samples taken at Adventfjorden in the western part of the Svalbard Archipelago were used as a test dataset to assess the transferability to other nearshore areas in the Arctic.

HIQ is surrounded by the Yukon Coast nearshore waters, which are part of the Canadian Beaufort Shelf (Fig. 1). The Mackenzie River is the main freshwater source of the Canadian Beaufort Shelf (Hill et al., 1991). The Mackenzie freshet in May marks the beginning of the ice break-up at the shelf with a peak discharge of up to 35000 m^3/s (O'Brien et al., 2006; Yang et al., 2015). Coastal erosion at HIQ occurs mostly during the open-water season, when the sea is not covered by ice, which typically spans from mid-June to late September (Solomon, 2005). However, single storm events can cause up to 43% of annual coastal erosion in the area (Lim et al., 2020). Coastal permafrost along the Yukon Coast in this region is rich in buried organic material (total organic Carbon content: 4.7 wt%, Mackay, 1971; Tanski et al., 2017) and has high ice content, which occupies ~46% of the ground volume, making it especially vulnerable to increasing air temperatures. Coastal morphology covers a wide range of features, from sandy beaches towards the South of the island, permafrost cliffs with heights up to 30 m towards the North and West of HIQ, and retrogressive thaw slumps, which are most common towards the SE (Obu et al., 2016). Sediments consist of mostly fine silt and clay particles, with varying amounts of sand (Fritz et al., 2012; Jong et al., 2020).

The climate in the southern Beaufort Sea is characterized by long winters and short summers (Burn and Zhang, 2009). The predominant wind directions during the open water season are ESE and NW (Hill et al., 1991; Radosavljevic et al., 2015). During ESE wind conditions, the Mackenzie River plume has the potential to reach the nearshore waters of HIQ, which results in higher suspended sediment concentration and water temperatures (Klein et al., 2019). Wind direction and wind speed further influence hydrodynamics such as currents (Hill et al., 1991) and upwelling (Williams et al., 2006).

Adventfjorden is a small side-arm of Isfjorden in western Svalbard (Fig. 2). This fjord has a partially glaciated catchment, and receives large inorganic sediment loads from several land-terminating glaciers during the melt season (from June–September), especially via the Longyearelva and Adventelva rivers (Nowak et al., 2019; Węsławski et al., 2011; Zajaczkowski and Włodarska-Kowalczuk, 2007). These river plumes, rich of inorganic sediment loads from a glacially-influenced catchment, provide a strong contrast from the organic-rich sediments and coastal erosion that are key features of the HIQ system. The climate at Svalbard is characterized by long, cold winters and short summers. The warm West Spitsbergen Current significantly increases air temperature in the western part of Svalbard, including Adventfjorden, enhancing glacial melt during summer and thus sediment export to the fjord (Hanssen-Bauer et al., 2019; Nowak et al., 2019).

2.2. In-situ sampling

In-situ samples of SPM concentration and turbidity measurements were collected around HIQ between July 29th and August 15th, 2018 and between July 30th and August 8th, 2019 (for detailed information, see supplementary information). Water leaving reflectance was only measured during summer season 2019. Samples were collected along transects perpendicular to the coastline of HIQ and the nearby Yukon coast (Fig. 1). Each transect consisted of five individual sampling locations with distances of 50 m, 250 m, 500 m, 1000 m, and 2000 m to the

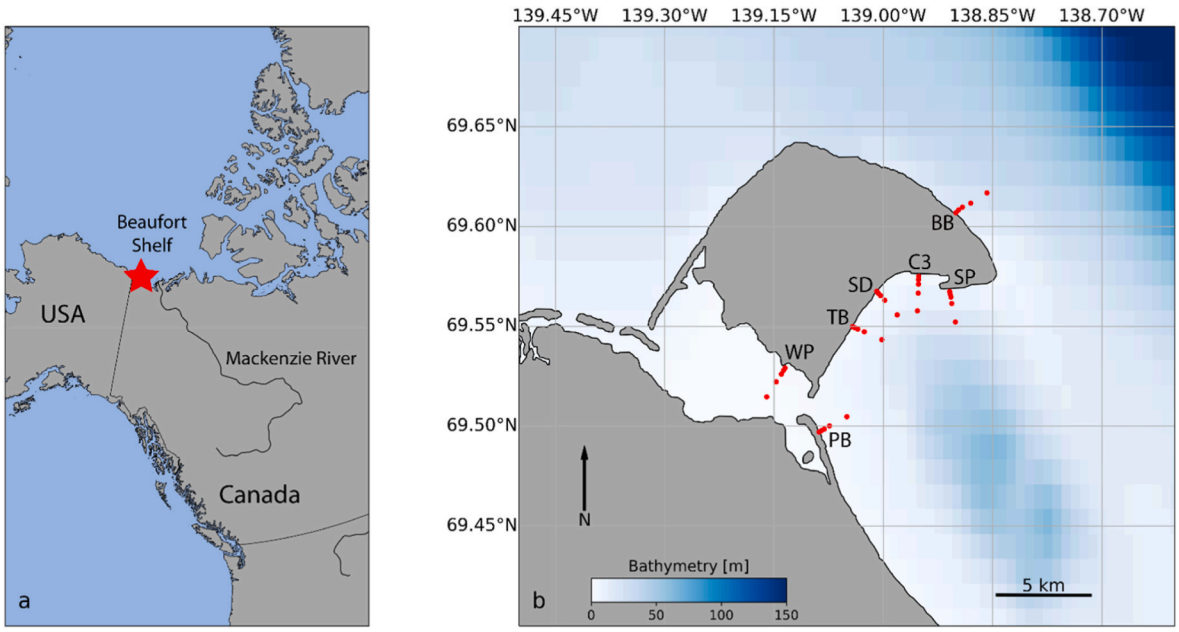

Fig. 1. (a) Location of the study area on the Canadian Beaufort Shelf, near the northernmost border of Canada and the USA. (b) Close-up to Herschel Island Qikuqtaruk. Sampling transects during the 2019 field campaign are indicated by red dots. (For interpretation of the references to color in this figure legend, the reader is referred to the Web version of this article.)

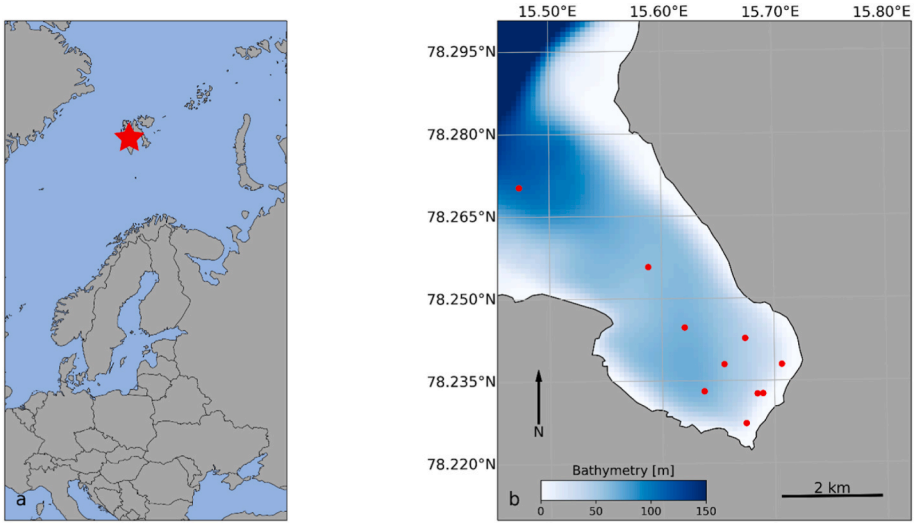

Fig. 2. (a) Location of Adventfjorden, a small sidearm of the Isfjorden system on the west coast of Svalbard. (b) Close-up of Adventfjorden, with the sampling grid indicated by red dots. (For interpretation of the references to color in this figure legend, the reader is referred to the Web version of this article.)

coastline, respectively. Samples were taken from onboard a Zodiac MKV HD. The transects were designed to resolve different types of nearshore morphologies and processes: transects PB and WP were influenced by longshore currents and adjacent lagoons; transects TB, SD, and C3 were located close to the outlets of retrogressive thaw slumps and creeks; and transects SP and BB were located in front of eroding permafrost cliffs (Fig. 1).

SPM concentrations at each sampling location were calculated from three individual water samples, which were taken in 5 cm water depth in rinsed Nalgene 1L bottles. They were filtered through pre-weighed Whatman GF/F 47 mm glass microfiber filters in field camp right after the sampling. The filters were dried at 50 °C in the laboratory for five days prior to re-weighing to calculate SPM concentrations. SPM concentrations were corrected for salt remnants based on the results presented by Neukermans et al. (2012). Turbidity was measured by taking a water sample in a 10 ml pre-rinsed glass vial at a water depth of 5 cm and analyzing it in a HACH 2100Q turbidity meter. Duplicate samples were taken and measured at each sampling location and then averaged.

Water-leaving reflectance was measured above the water surface using two hyperspectral TriOS RAMSES radiometers, one of each measuring radiance (L, [W/(m^2*sr)]) and irradiance (E, [W/(m^2)]) in the spectral range of 350–950 nm at a spectral resolution of 4 nm. Each radiometric measurement sequence lasted for 5 min. While the downwelling sky-irradiance (E_D) was sampled throughout the complete 5 min pointing the zenith at the highest location of the coastal ship, the radiance was measured as total upwelling (L_U) and sky radiances (L_D), respectively, for 2 min each. Radiance measurements were taken in 135° relative to the solar zenith angle and in nadir/zenith angles of 40° (Mobley, 1999).

In-situ turbidity measurements in Adventfjorden were taken on June

14th, 2019, and August 8th, 2019, to match Sentinel 2 data acquisitions. 10 locations were sampled on both dates (Fig. 2). Triplicate measurements were conducted using a Thermo-Eutech TN-100 turbidity meter.

2.3. Optical data processing

TriOS RAMSES measurements were analyzed according to Ruddick et al. (2006) and then used to calculate the remote sensing reflectance (R_{RS}) according to Mobley (1999). Prior to the analysis, measurements were discarded if one of the following conditions was met: (i) the inclination in either x or y direction was larger than 5°; (ii) either E_D, L_U or L_D differed by more than 25% at 550 nm to a neighboring scan; or (iii) spectra were incomplete due to a sensor malfunction (Ruddick et al., 2006). In total, measurements from 32 sampling locations met the quality requirements. Next, the first five consecutive scans of each E_D, L_U and L_D were used to calculate five separate instances of RRS according to equation (1):

$$R_{RS}(\lambda) = \frac{L_U - \rho^* L_D}{E_D} \quad (1)$$

The ρ value, which represents the sky radiance reflection, was set according to Mobley (1999) depending on the cloud conditions during the sampling. The ρ value covers a range of 0.035–0.07, representing varying coverages of cumulus clouds at the horizon during the sampling. For one measurement, a ρ value of 0.13 was assigned due to the occurrence of a larger cloud band at the horizon. Additionally, a baseline correction was conducted for measurements that corresponded to low turbidity measurements as proposed in Knaeps et al. (2015), which was adopted to lower wavelengths. Briefly, the R_{RS} in wavelengths above 900 nm was assumed to be 0 if the turbidity measurement of the same location were below 10 FNU (Jain and Singh, 2003), and then used as baseline. The resulting five separate instances of R_{RS} were used to calculate means, medians, and standard deviations of R_{RS}. Hereafter, R_{RS} always refers to the mean value of the five separate instances of R_{RS} after skylight correction and baseline correction (if conducted). R_{RS} was converted to water leaving reflectance (R_W, $R_W = R_{RS} * \pi$) prior to relating it to surface turbidity (Fig. 3).

2.4. Algorithm tuning

To create the ANTA based on multiple operating and historical satellite sensors, relative spectral response functions of Landsat 4/5 TM, 7 ETM+ and 8 OLI, Sentinel 2 MSI, MODIS Aqua, and Sentinel 3 OLCI were used as relative means to calculate a single R_{RS} value for each satellite sensor spectral band.

32 measurements of R_{RS} and turbidity from summer 2019 at HIQ were used to calibrate a reflectance-turbidity relationship based on Nechad et al. (2009) and Dogliotti et al. (2015). The general semi-empirical relationship in order to retrieve the turbidity (T(λ)) can be written as

$$T(\lambda) = \frac{A(\lambda)^*\rho(\lambda)}{\left(\frac{1-\rho(\lambda)}{C(\lambda)}\right)} \quad (2)$$

where ρ is the water leaving reflectance (R_W) at wavelength λ, and A [FNU] and C being wavelength dependent constants. According to Dogliotti et al., (2015), T(red) was used if $R_W(red) < 0.05$ and T(NIR) if $R_W(red) > 0.07$, with a linear blending in the transition. The A and C parameters were calculated for R_W(red) and R_W(NIR) using non-linear least-square regression for each of the above named sensors (Table 1).

The performance of the ANTA was compared to the original semi-empirical turbidity algorithm presented in Dogliotti et al. (2015) by applying both algorithms to the dataset presented by (Klein et al., 2019) that consists of 35 Scenes of the HIQ nearshore zone recorded by Landsat TM, ETM+ and OLI between 1986 and 2016. The 35 scenes were grouped based on their prevailing wind conditions (changing winds, NW, and ESE (Klein et al., 2019), to calculate mean turbidity per used algorithm and wind condition.

2.5. Satellite imagery processing

In this study, four scenes recorded on June 21, 2019 within 76 min, one of each taken by Landsat 8, Sentinel 2A, Sentinel 3A, and Sentinel 3B were compared to analyze the performance of the turbidity-reflectance relationship applied to the different satellite sensors. These scenes

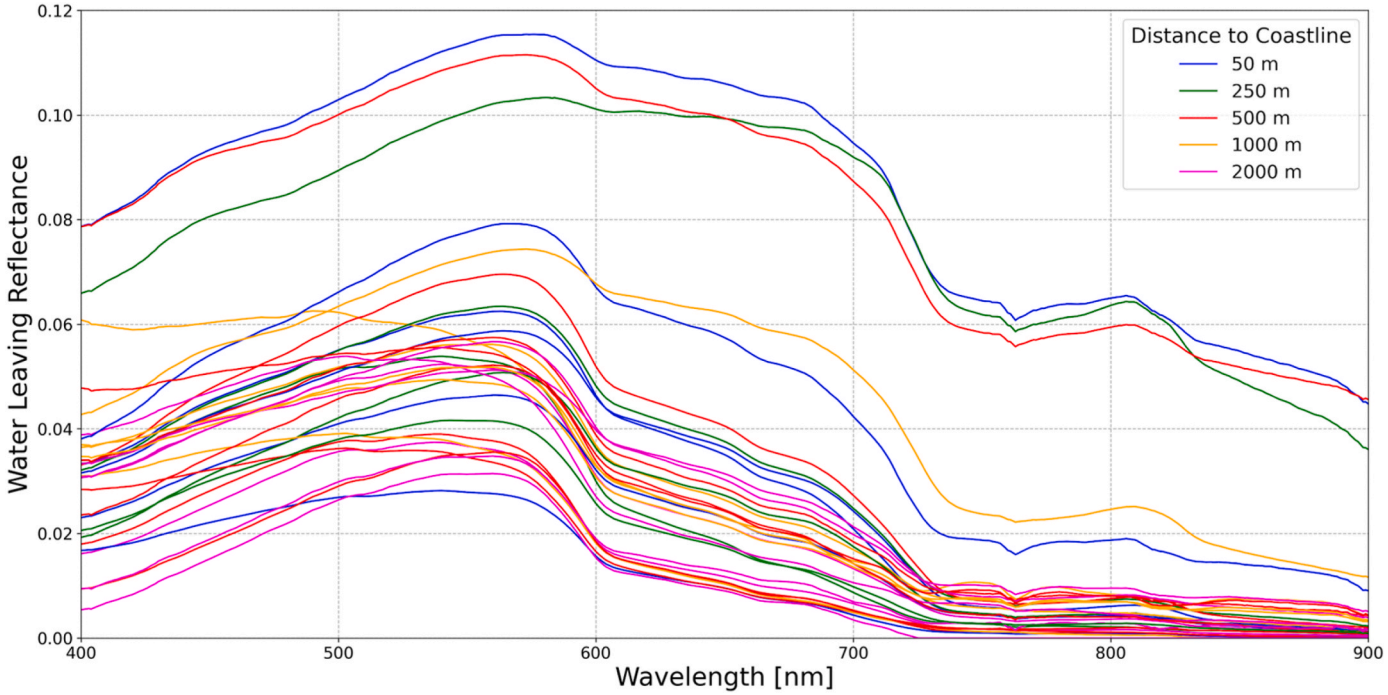

Fig. 3. In-situ measured spectra of water leaving reflectance ($R_{RS}*\pi$) that were used for the calibration of the turbidity algorithm. Spectra were measured using two TriOS Ramses hyperspectral radiometers above the water surface.

Table 1
Calibration coefficients A [FNU] and C for multiple operative and historical satellite sensors to be used in their respective red and NIR wavelength spectral bands. Coefficients published by Dogliotti et al. (2015) and Nechad et al. (2016) are given as reference.

Sensor	Wavelength	Center Wavelength [nm]	A [FNU]	C
Landsat 4/5 TM	red	660	283.43	0.1395
	NIR	839	1528.7	0.2124
Landsat 7 (ETM+)	red	661	282.54	0.1395
	NIR	835	1546.7	0.2119
Landsat 8 (OLI)	red	655	268.61	0.1401
	NIR	865	2159.3	0.2093
Sentinel 2 (MSI)	red	665	288.95	0.1395
	NIR	865	1830.7	0.2033
Sentinel 3 (OLCI)	red	665	221.03	0.1233
	NIR	865	1613.0	0.1638
MODIS Aqua	red	659	260.15	0.1396
	NIR	865	1760.1	0.205
MODIS (Dogliotti et al., 2015)	red		228.1	0.1641
	NIR		3078.9	0.2112
Landsat 8 (Nechad et al., 2016)	red		526.82	0.2365
	NIR		3031.7	0.2114

were chosen because this was the only time during the 2019 summer season when all 4 sensors recorded a scene of HIQ within this short time difference (Table 2).

To test the ANTA, two scenes were used which correspond to match-up in-situ measurements of turbidity in Adventfjorden, Svalbard. One scene was recorded on June 14th by Sentinel 2A and one on August 8th, 2019 by Sentinel 2B. Match-up scenes for Landsat 8 are not available, and the spatial resolution of Sentinel 3 is not sufficient to resolve the small-scale sampling grid (Fig. 2).

Landsat imagery was downloaded from the United States Geological Service (USGS) Earth Explorer as Level1T product, which means with georeferencing but without atmospheric correction. Sentinel 2 and Sentinel 3 imagery was downloaded from the European Space Agency (ESA) Copernicus Hub as Level1C product. Atmospheric correction towards water leaving reflectance (R_W) was performed using the ACOLITE software version 20210114.0 (Landsat 8 and Sentinel 2, Vanhellemont, 2019; Vanhellemont and Ruddick, 2018) and the ACOLITE software version 20210421.0 (Sentinel 3, Generic Public Beta, Vanhellemont and Ruddick, 2021) applying the dark spectrum fitting algorithm, which was found to perform best in coastal environments (Renosh et al., 2020; Vanhellemont and Ruddick, 2021).

3. Results and discussion

3.1. Turbidity and SPM

The values of in-situ turbidity in the nearshore area varied from 0.83 FNU to 176 FNU, with a mean value of 15.95 FNU and a median of 5.02 FNU. SPM values taken at the same location varied from 6.2 g/m^3 to 190.2 g/m^3, with a mean value of 26.1 g/m^3 and a median of 16.61 g/m^3 (for detailed information, see supplementary data). The strong relation between turbidity and SPM concentration is linear ($R^2 = 0.93$, Fig. 4). Each of the measured transects (Fig. 1) showed highest turbidity and SPM close to the coast, where the influence of coastal erosion and resuspension is highest. Fig. 4 reveals that SPM concentrations below 10 g/m^3 are only rarely measured, as well as turbidity being higher than the SPM measurement from the same location.

The linearity of this relationship was expected, as turbidity is defined as the measurement of light scattering, which is caused by suspended material (ISO 7027), and is similar to recently reported results from various regions on earth (Jafar-Sidik et al., 2017; Sent et al., 2020; Xue et al., 2019) that show the almost linear relationship between backscatter measurements and sediment. The offset towards SPM concentrations, however, has only rarely been reported in the literature. Bhargava and Mariam (1990) reproduced a similar result during a lab experiment. It is shown that the turbidity of suspended clay samples stays relatively low with increasing SPM concentrations. The authors identify organic content as the main damping factor for turbidity, which also darkens the sediment. This matches recent field observations: water that is strongly affected by release of particulate organic carbon (POC) and dissolved organic matter (DOC) from permafrost are brown-yellowish. This is caused by the dominance of light absorption by non-algal-particles (aNAP) and colored dissolved organic matter (aCDOM). The fraction of organic carbon (OC) that is released in its particulate fraction (POC) is substantially higher from coastal erosion compared to riverine transport, where most of the OC is released as dissolved organic carbon (Gordeev and Kravchishina, 2009; McClelland et al., 2016).

3.2. ANTA performance

The application of the ANTA reveals both a high sensitivity towards low and high turbidity features for all tested sensors (Fig. 5). Generally, the retrieved values using the Landsat 8 (Fig. 5a) and Sentinel 2 (Fig. 5) imagery are higher than for using the Sentinel 3 imagery (Fig. 5c and d), which is mainly caused by the differences in spatial resolution (30 m, 20 m, and 300 m, respectively). All sensors resolve the highest turbidity values close to the shoreline of HIQ in their respective result image, with values above 150 FNU modeled at the NE coast of HIQ for Landsat 8 and Sentinel 2.

Both Landsat 8 and Sentinel 2 are able to resolve a narrow band of high turbidity in the direct vicinity of the HIQ coastline, especially along the NE and NW coast. This band of high turbidity is caused by high erosional input from the adjacent permafrost cliffs, which are exposed to the maximum wave energy, as well as longshore sediment transport during ESE wind conditions. Recent research (Klein et al., 2019) has identified a broad band of high turbidity around the whole island, independent from the wind forcing. The high turbidity band is narrower than reported in Klein et al. (2019), which might be due to an earlier recording of the imagery in this study; most data used in Klein et al., (2019) was recorded in July and August, when temperatures and thus thermo-erosion are usually higher. This is in line with recent modelling approaches (Nielsen et al., 2020; Rolph et al., 2021), which identify thermal forcing through increasing air and water temperature as the main driver of coastal erosion along permafrost coasts. This in turn has the potential to release large amounts of greenhouse gases to the atmosphere (Tanski et al., 2021), further enhancing climate warming.

For turbidity values below 10 FNU, turbidity values retrieved by Landsat 8 satellite imagery are lower than the Sentinel 2 retrieved turbidity (Fig. 6), which gets closer to the collected field data. However, even Landsat 8 is unable to reflect the lowest in-situ turbidity, which were between 2 and 4 FNU during the whole summer season (see supplementary data for more information). As a result, Landsat 8 retrieved turbidity has a higher contrast for higher turbidity values (above 10 FNU), which is an asset when it comes to the identification of sediment ejections towards the offshore, sediment pathways, and filaments.

Sediment ejections towards offshore waters are most prominent along the NE and SE coasts of the island. The feature along the NE coast is most likely caused by upwelling, which is very common in this area (Williams et al., 2006). Colder and nutrient rich water from outside the Canadian Beaufort Shelf rises to the ocean surface N of HIQ, and the

Table 2
Specifications of the used satellite imagery.

Satellite	Date	Time (UTC)	Identifier
Sentinel 3B	June 21st, 2019	19:59	0179_026_356_1800_MAR_O_NT
Sentinel 3A	June 21st, 2019	20:39	0179_046_114_1800_MAR_O_NT
Landsat 8	June 21st, 2019	20:58	LC80670112019172LGN00
Sentinel 2A	June 21st, 2019	21:15	N0207_R143_T07WET

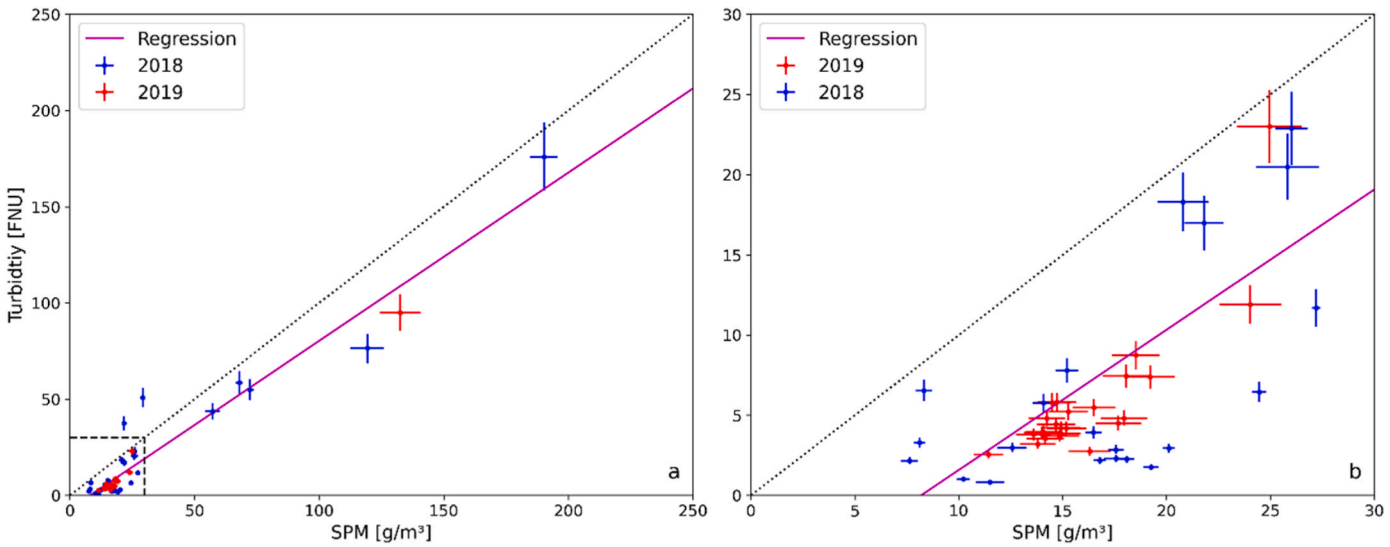

Fig. 4. (a) Turbidity and SPM measurements from 2018 to 2019 including error bars and (b) zoom into the lower value range. The turbidity error was assigned to 10% of the measurement, which is the margin of error of the turbidity meter as provided by the manufacturer. SPM error was calculated as the standard deviation of triplicate samples.

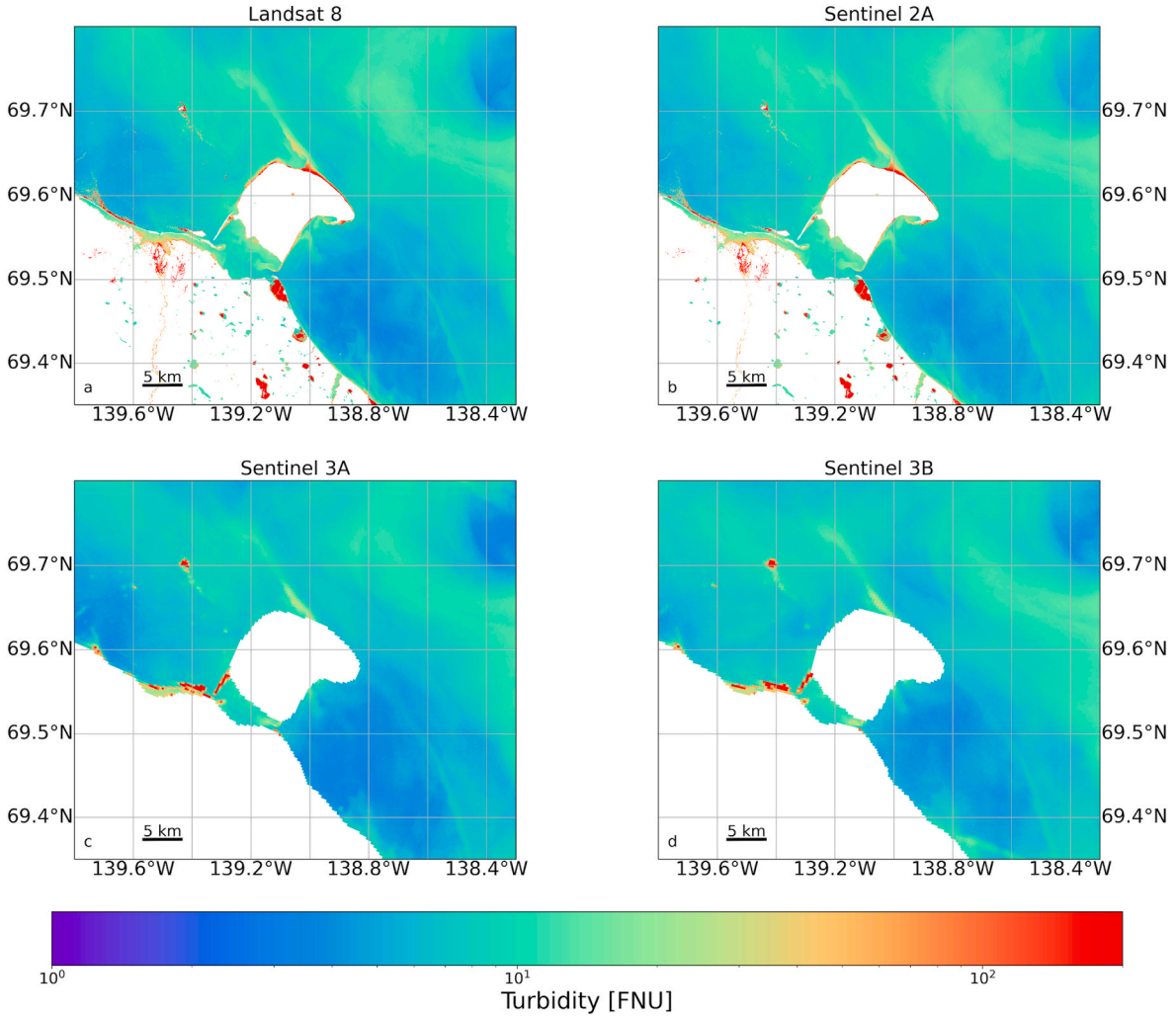

Fig. 5. Application of the ANTA to different satellite data recorded at June 19th, 2019 (Table 1): (a) Landsat 8, (b) Sentinel 2A, (c) Sentinel 3A, (d) Sentinel 3B.

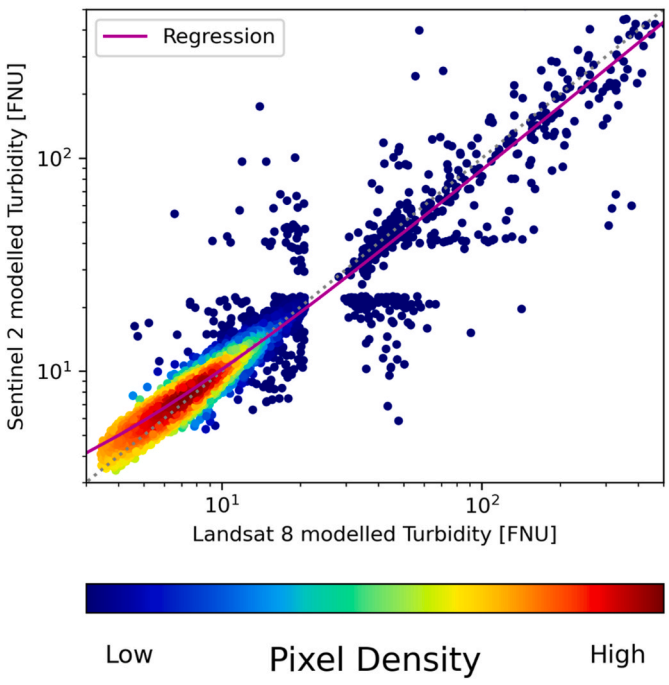

Fig. 6. Scatterplot between Landsat 8 and Sentinel 2 derived turbidity. 3000 randomly generated points in the extent of Fig. 5 a and b (excluding land areas) were used for the comparison. The regression line is linear (R^2 = 0.89, y = 0.87x + 1.94) and shows the overestimation of Sentinel 2 derived turbidity below 10 FNU.

Coriolis Force directs the sediment rich longshore current towards the offshore. The observation of sediment ejections along the SE coast of HIQ is in line with the occurrence of high sediment producing erosional features, such as the largest creek of the island, and retrogressive thaw slumps (Lantuit and Pollard, 2008; Obu et al., 2016). These features are not permanent, but are caused by extreme events, when increased air temperatures lead to higher thermo-erosion of the coastal permafrost (Weege, 2016). Turbid filaments are also resolved along the Yukon coast, best visible SE of HIQ.

Sentinel 3A and Sentinel 3B retrieved turbidity values differ from those retrieved using Landsat 8 and Sentinel 2 data substantially due to their lower spatial but higher spectral and temporal resolution. Due to their high spatial resolution, Sentinel 2 and Landsat 8 were able to resolve small scale features of turbid filaments in the nearshore zone around Herschel Island. The spatial resolution of Sentinel 3 (300 m) is not sufficient to resolve these features (Fig. 5c and d). However, this is not true for the sediment ejection features along the NE and SE coast of HIQ. Besides the turbulent nearshore waters in direct vicinity of the coastline, both Sentinel 3A and 3B derived turbidity resolves a similar range of turbidity as Landsat 8.

3.3. *Comparison with the Dogliotti et al. (2015) algorithm*

The performance of the ANTA was compared to the widely applied semi-empirical relationship presented in Dogliotti et al. (2015, Fig. 7). A general comparison reveals substantial differences, which includes higher sensitivity towards low turbidity values (best visible in Fig. 7e), and an overestimation of intermediate turbidity values (20–50 FNU, best visible in Fig. 7f). The largest differences are resolved in the comparison of the NW wind situation (Fig. 7b and e). The ANTA is able to resolve turbidity values below 2 FNU towards the N and W of HIQ, which the Dogliotti et al. (2015) algorithm is not able to (Fig. 8b). Additionally,

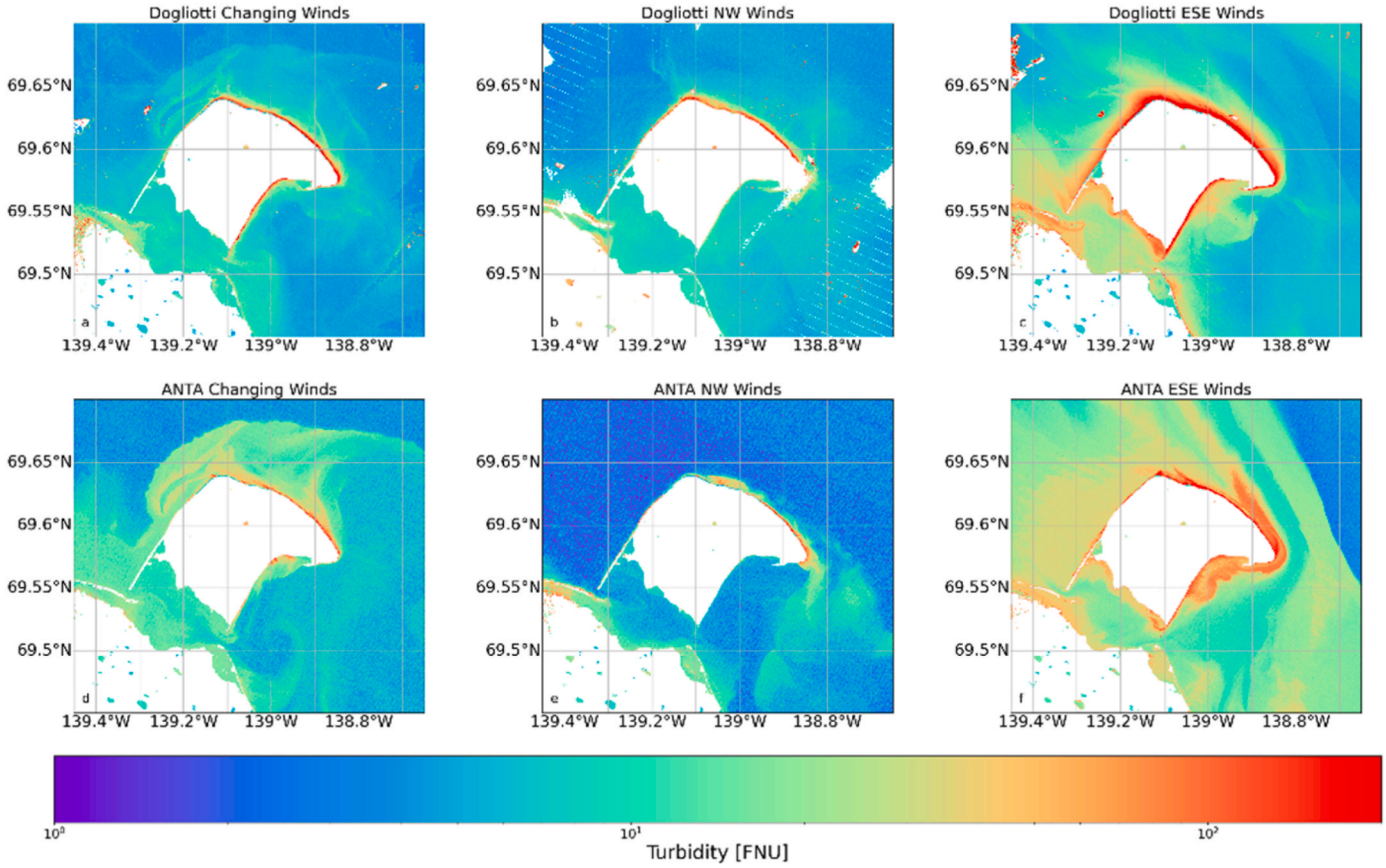

Fig. 7. Comparison of the ANTA to the results presented in Klein et al. (2019) applying the Dogliotti et al. (2015) algorithm.

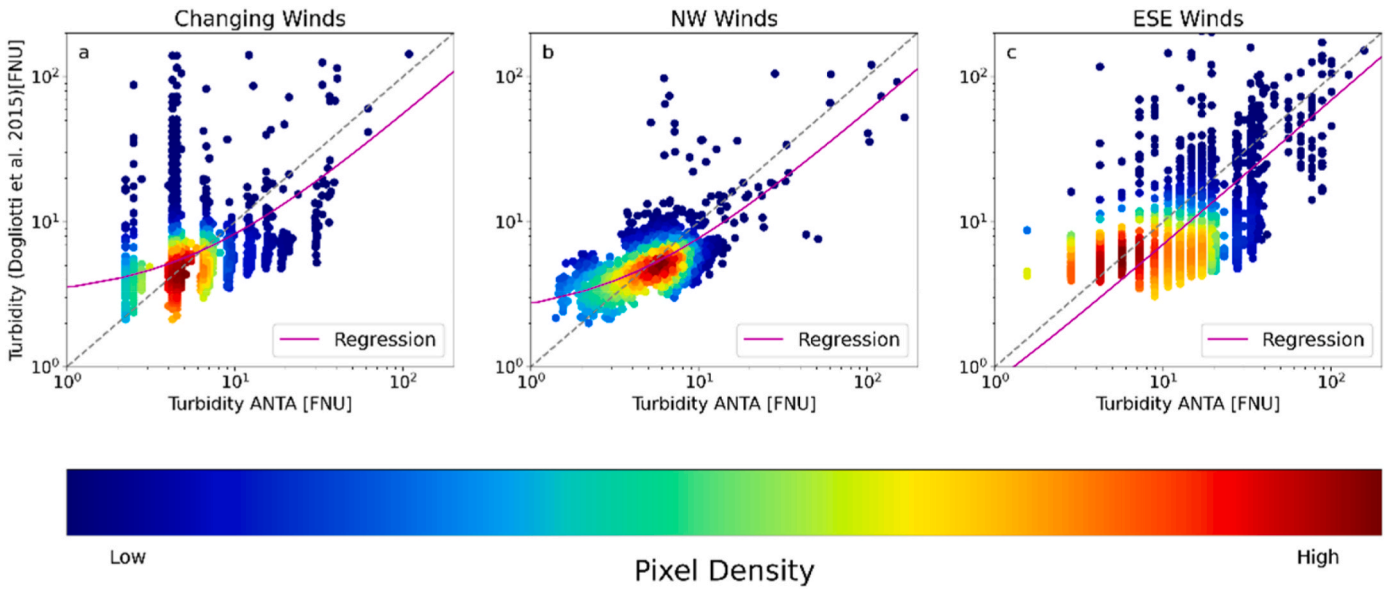

Fig. 8. Scatterplot comparing the different turbidity algorithms shown in Fig. 7.

longshore drift features towards the SE, which are well resolved in Fig. 7e, are not resolved at all in Fig. 7b. The scatterplot comparing both images (Fig. 8b) supports these observations. The lowest turbidity values are overestimated by the Dogliotti et al. (2015) algorithm. In the current study, the majority of data points fall within the range of 5–8 FNU, which both algorithms resolve similarly.

During ESE wind conditions, the general patterns of longshore drift towards NW is resolved by both algorithms (Fig. 7c and f). In the Dogliotti et al. (2015) algorithm (Fig. 7c), turbidity values are higher in the immediate vicinity of the coastline, but decrease more rapidly to values of approximately 10 FNU compared to the ANTA (Fig. 7f). Along the NE coast of HIQ, the ANTA resolves sediment pathways towards the offshore, which are not resolved in the Dogliotti et al. (2015) algorithm. The ANTA resolves a filament of increased turbidity NE of HIQ, which indicates external influences, most likely by the Mackenzie River. Sediment ejections due to larger erosional events along the SE coast of HIQ are resolved by both models. The Dogliotti et al. (2015) algorithm indicates longshore drift through the Workboat Passage between HIQ and the Yukon main land towards the NW, which is not resolved in the ANTA (Fig. 7f). The scatterplot in Fig. 8c shows similar patterns as in Fig. 8b: lowest turbidity values are modeled higher in the Dogliotti et al. (2015) algorithm, which changes with increasing turbidity. Turbidity values between 10 and 40 FNU are modeled higher by the ANTA, while values around 100 FNU and above are modeled similarly by both algorithms.

During changing wind conditions (Fig. 7a and d), both algorithms resolve a mixture of the features which are also well-captured during NW and ESE wind conditions. The ANTA resolves a near-circular filament feature ranging from the W to the NE coast of HIQ, as well as 2 sediment pathways offshore along the NE coast (Fig. 7d), both of which tend to disappear in Fig. 7a. The ANTA also resolves an eddy-like feature S of HIQ. The scatterplot comparing the two algorithms (Fig. 8a) reveals remarkably higher turbidity values modeled by the Dogliotti et al. (2015) algorithm when the ANTA modeled values ~ 3–5 FNU. Turbidity values between 10 and 30 FNU modeled by the ANTA are nearly exclusively modeled below 10 FNU by the Dogliotti et al. (2015) algorithm, showing similar patterns like in Fig. 8c.

Comparing the data to field observations from 2018 to 2019, where turbidity values were frequently below 5 FNU, the ANTA has a superior performance in resolving turbidity values this low. The Dogliotti et al. (2015) algorithm models higher turbidity values above 200 FNU compared to the ANTA, which is remarkably higher than each measurement taken during the two summer seasons. Based on this comparison, the ANTA shows the best performance in the low-to intermediate turbidity values (below 50 FNU), when identifying filaments of higher turbidity and sediment pathways along- or offshore.

3.4. *Test and transfer of the ANTA*

In-situ surface turbidity data from Adventfjorden were used as test data to evaluate the performance of the ANTA developed for the HIQ nearshore area for another nearshore Arctic coastal area. Fig. 9 shows that the ANTA is capable of resolving both low and high turbidity values. Sediment pathways and filaments of high turbidity are well resolved close to the river outlet in the SE part of Adventfjorden, as well as in the NW towards Isfjorden. The results reveal that lowest turbidity values (up to ~ 10 FNU) are typically overestimated (Fig. 10), which is similar to the results obtained from the HIQ imagery. This feature is related to the Sentinel 2 sensor design: it was designed to focus on land applications and the reflectance over low-turbidity waters are much lower than over land. Values between 10 and 50 FNU are accurately retrieved, while higher values are overestimated, which may reflect the much higher inorganic contribution to the SPM in Adventfjorden compared to HIQ. The ANTA performs reasonably well considering the strong differences in sediment composition between HIQ and Adventfjorden. During the summer melt season, suspended sediments in Adventfjorden are primarily delivered by rivers fed by land-terminating glaciers, leading to a high inorganic contribution to the SPM, and distinct river plumes extending into the fjord (Zajaczkowski and Włodarska-Kowalczuk, 2007). The good performance of the ANTA at this contrasting site may in part reflect the fact that the test data were collected in early and late summer, outside of the period of highest glacial melt, and where SPM often includes a higher contribution of organic matter (Walch, 2021, Poste *unpublished data*).

Given that the environmental conditions in Adventfjorden differ strongly from those at Herschel Island, the algorithm performs reasonably well. As Adventfjorden is influenced by glacial discharge, the fjord receives larger freshwater input than the HIQ nearshore waters (Nowak et al., 2019). Together with the different optical properties of inorganic suspended material in contrast to the organic rich material at HIQ (Gould et al., 2002), the ANTA proved to be robust and transferable. This suggests at least some degree of applicability of the ANTA algorithm for Arctic nearshore environments beyond HIQ. However, it is noted that the ANTA should be used with caution in environments with high

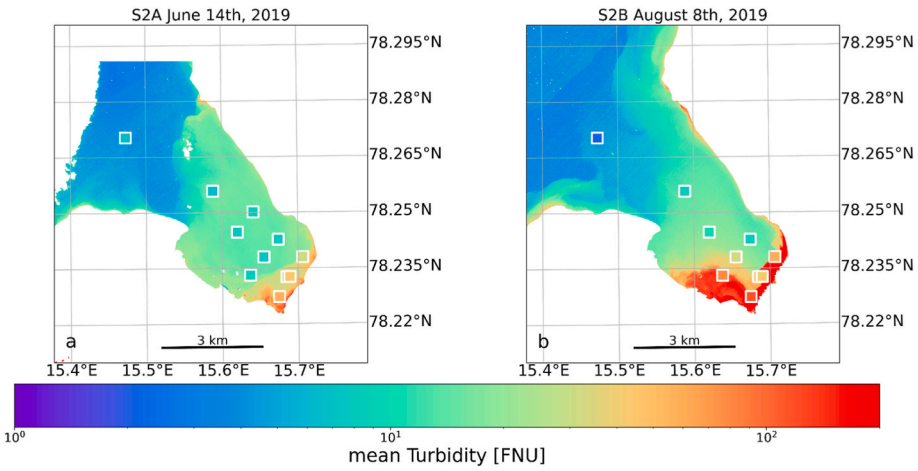

Fig. 9. Application of the ANTA to Sentinel 2 imagery in Adventfjorden with in-situ turbidity measurements from the FreshFate sampling plotted in squares.

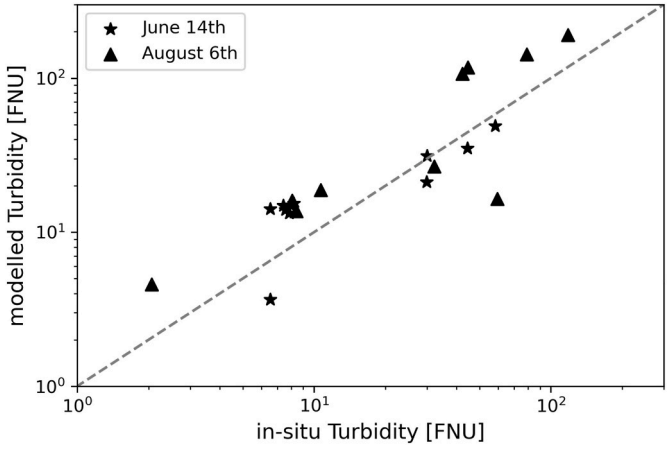

Fig. 10. Scatterplot comparing in-situ turbidity sampled in Adventfjord and Sentinel 2 derived turbidity values (ANTA).

freshwater input such as river deltas or glacial influenced areas during maximum melt season in summer, as they might add a higher level of optical complexity (Aurin and Dierssen, 2012), which the ANTA might not reflect accurately. The best performance is expected close to strongly eroding permafrost coasts with high organic carbon content, where conditions are likely to be more similar to those at HIQ.

4. Conclusion

The aim of this study was to improve nearshore satellite-based turbidity retrieval in Arctic nearshore environments. Therefore, in-situ measurements of turbidity, SPM concentration and water-leaving reflectance, collected in summer seasons 2018 and 2019 around Herschel Island Qikiqtaruk were used to calibrate the Arctic Nearshore Turbidity Algorithm (ANTA), a multi-sensor turbidity-reflectance relationship. The application of the ANTA to multiple operating sensors showed satisfactory results, improving on the Dogliotti et al. (2015) general algorithm for Arctic nearshore waters. Improvements included high sensitivity towards both low and high turbidity values, as well as resolving sediment pathways and filaments. Landsat 8 showed best capability to resolve turbid filaments and sediment pathways due to its higher sensitivity towards low turbidity values compared to Sentinel 2 and higher spatial resolution compared to Sentinel 3.

The ANTA was applied to Sentinel 2 imagery from Adventfjorden in Svalbard to assess its performance outside the Canadian Beaufort Sea, where the calibration data was collected. Despite strong differences in sources and distribution of suspended sediments between these sites, with Adventfjord being impacted by higher freshwater and inorganic sediment inputs from land-terminating glaciers, the ANTA proved to be robust and transferable. However, future research has to focus on the influence of the SPM particle size distribution and composition on the ANTA, and on the influence of organic content. Since high cDOM concentrations generally correlate with high freshwater input, it is recommended to use the turbidity algorithm with caution in the vicinity of large river deltas. The best performance is expected close to strongly eroding coasts with high organic Carbon content, where conditions are likely to be comparable to Herschel Island Qikiqtaruk, where the calibration data was collected. Comparing the ANTA to the widely used algorithm published by Dogliotti et al. (2015), higher detail was resolved in the nearshore area of Herschel Island Qikiqtaruk and shows the potential of this tuned algorithm for arctic nearshore waters.

In this study, the first turbidity-reflectance relationship specifically calibrated to Arctic nearshore environments is presented. It can be applied to a series of operating and historic satellite sensors. It is shown that improvements were made for identifying turbid filaments and sediment pathways along- and offshore when comparing it to globally used turbidity algorithms. The applicability of the ANTA in other Arctic nearshore environments was also clearly demonstrated, however, careful verification of the results is recommended due to scarce validation dataset availability.

As the Arctic will continue to be impacted by global climate change, coastal erosion and river sediment input to the nearshore zone will rise, too. Future implementations of chlorophyll or particulate organic carbon measurements will help to estimate the Carbon and nutrient supply of coastal erosion to Arctic nearshore waters. The implementation of machine-learning based data analysis will improve the efficiency of the algorithm. Additional pan-Arctic sampling campaigns and comparative studies could help strengthen the algorithm by increasing its accuracy in a variety of different settings.

Funding

This publication is part of the Nunataryuk project. The project has received funding under the European Union's Horizon 2020 Research and Innovation Program under grant agreement no. 773421. K.P.K. was financially supported by a Ph.D. stipend by the University of Potsdam (PoGS Potsdam Graduate School) and a short-term stipend by the German Academic Exchange Service (DAAD). I.N. was funded by the HGF AI-CORE, ESA CCI + Permafrost, and NSF Permafrost Discovery Gateway (NSF Grants #2052107 and #1927872) projects. BJ was funded by the European Space Agency (ESA) as part of the Climate Change Initiative (CCI) fellowship (ESA ESRIN/Contract No. 4000l3376l/2l/I-

NB). The work in Adventfjord was supported by the Research Council of Norway ('TerrACE' project; project number 268458), and the Fram Center for High North Research "Fjord and Coast" flagship ('FreshFate' project; project number 132019).

Declaration of competing interest

The authors declare that they have no known competing financial interests or personal relationships that could have appeared to influence the work reported in this paper.

Acknowledgments

USGS and NASA are acknowledged for Landsat imagery. ESA is acknowledged for Sentinel 2 and 3 imagery. We thank Bernard Gentili for his help when processing TriOS RAMSES data and Maeve McGovern for his involvement in field and lab work in Adventfjord. We acknowledge the support of Deutsche Forschungsgemeinschaft (German Research Foundation) and Open Access Publication Fund of University of Potsdam.

Appendix A. Supplementary data

Supplementary data to this article can be found online at https://doi.org/10.1016/j.srs.2021.100036.

References

Aurin, D.A., Dierssen, H.M., 2012. Advantages and limitations of ocean color remote sensing in CDOM-dominated, mineral-rich coastal and estuarine waters. Remote Sens. Environ. 125, 181–197. https://doi.org/10.1016/j.rse.2012.07.001.

Bhargava, D.S., Mariam, D.W., 1990. Spectral reflectance relationships to turbidity generated by different clay materials. Photogramm. Eng. Rem. Sens. 56, 225–229.

Biskaborn, B.K., Smith, S.L., Noetzli, J., Matthes, H., Vieira, G., Streletskiy, D.A., Schoeneich, P., Romanovsky, V.E., Lewkowicz, A.G., Abramov, A., Allard, M., Boike, J., Cable, W.L., Christiansen, H.H., Delaloye, R., Diekmann, B., Drozdov, D., Etzelmüller, B., Grosse, G., Guglielmin, M., Ingeman-Nielsen, T., Isaksen, K., Ishikawa, M., Johansson, M., Johannsson, H., Joo, A., Kaverin, D., Kholodov, A., Konstantinov, P., Kröger, T., Lambiel, C., Lanckman, J.P., Luo, D., Malkova, G., Meiklejohn, I., Moskalenko, N., Oliva, M., Phillips, M., Ramos, M., Sannel, A.B.K., Sergeev, D., Seybold, C., Skryabin, P., Vasiliev, A., Wu, Q., Yoshikawa, K., Zheleznyak, M., Lantuit, H., 2019. Permafrost is warming at a global scale. Nat. Commun. 10, 1–11. https://doi.org/10.1038/s41467-018-08240-4.

Burn, C.R., Zhang, Y., 2009. Permafrost and climate change at Herschel island (Qikiqtaruq), Yukon Territory , Canada. J. Geophys. Res. 114, 1–16. https://doi.org/10.1029/2008JF001087.

Carmack, E., Wassmann, P., 2006. Food webs and physical-biological coupling on pan-Arctic shelves: unifying concepts and comprehensive perspectives. Prog. Oceanogr. 71, 446–477. https://doi.org/10.1016/j.pocean.2006.10.004.

Constantin, S., Constantinescu, Ștefan, Doxaran, D., 2017. Long-term analysis of turbidity patterns in Danube Delta coastal area based on MODIS satellite data. J. Mar. Syst. 170, 10–21. https://doi.org/10.1016/j.jmarsys.2017.01.016.

Déry, S.J., Hernández-Henríquez, M.A., Burford, J.E., Wood, E.F., 2009. Observational evidence of an intensifying hydrological cycle in northern Canada. Geophys. Res. Lett. 36, 1–5. https://doi.org/10.1029/2009GL038852.

Dogliotti, A.I., Ruddick, K.G., Nechad, B., Doxaran, D., Knaeps, E., 2015. A single algorithm to retrieve turbidity from remotely-sensed data in all coastal and estuarine waters. Remote Sens. Environ. 156, 157–168. https://doi.org/10.1016/j.rse.2014.09.020.

Doxaran, D., Ehn, J., Bélanger, S., Matsuoka, A., Hooker, S., Babin, M., 2012. Optical characterisation of suspended particles in the Mackenzie River plume (Canadian Arctic Ocean) and implications for ocean colour remote sensing. Biogeosciences 9, 3213–3229. https://doi.org/10.5194/bg-9-3213-2012.

Dunton, K.H., Weingartner, T., Carmack, E.C., 2006. The nearshore western Beaufort Sea ecosystem: circulation and importance of terrestrial carbon in arctic coastal food webs. Prog. Oceanogr. 71, 362–378. https://doi.org/10.1016/j.pocean.2006.09.011.

Fritz, M., Vonk, J.E., Lantuit, H., 2017. Collapsing arctic coastlines. Nat. Clim. Change 7, 6–7. https://doi.org/10.1038/nclimate3188.

Fritz, M., Wetterich, S., Schirrmeister, L., Meyer, H., Lantuit, H., Preusser, F., Pollard, W. H., 2012. Eastern Beringia and beyond: late Wisconsinan and Holocene landscape dynamics along the Yukon coastal plain. Canada. Palaeogeogr. Palaeoclimatol. Palaeoecol. 319–320, 28–45. https://doi.org/10.1016/j.palaeo.2011.12.015.

Gordeev, V.V., Kravchishina, M.D., 2009. River flux of dissolved organic carbon (DOC) and particulate organic carbon (POC) to the Arctic Ocean: what are the consequences of the global changes? In: Nihoul, J.C.J., Kostianoy, A.G. (Eds.), Influence of Climate Change on the Changing Arctic and Sub-arctic Conditions. Springer, Dordrecht, Dordrecht, The Netherlands, pp. 145–160. https://doi.org/10.1007/978-1-4020-9460-6.

Gould, R.W., Stavn, R.H., Twardowski, M.S., Lamela, G., 2002. Partitioning optical properties into organic and inorganic components from ocean color imagery. In: Proceedings of the Ocean Optics XVI, pp. 1–10.

Groom, S.B., Sathyendranath, S., Ban, Y., Bernard, S., Brewin, B., Brotas, V., Brockmann, C., Chauhan, P., Choi, J.K., Chuprin, A., Ciavatta, S., Cipollini, P., Donlon, C., Franz, B.A., He, X., Hirata, T., Jackson, T., Kampel, M., Krasemann, H., Lavender, S.J., Pardo-Martinez, S., Melin, F., Platt, T., Santoleri, R., Skakala, J., Schaeffer, B., Smith, M., Steinmetz, F., Valente, A., Wang, M., 2019. Satellite ocean colour: current status and future perspective. Front. Mar. Sci. 6 https://doi.org/10.3389/fmars.2019.00485.

Hanssen-Bauer, I., Førland, E.J., Hisdal, H., Mayer, S., Sandø, A.B., Sorteberg, A., 2019. Climate in Svalbard 2100. NCSS Report No. 1/2019. Norwegian Centre of Climate Services (NCCS) for Norwegian Environment Agency (Miljødirektoratet), Trondheim, Norway.

Hill, P.R., Héquette, A., Ruz, M.-H., Jenner, K.A., 1991. Geological investigations of the Canadian Beaufort Sea coast. Geol. Surv. Canada, Open File Open File Rep. 2387.

Holmes, R.M., McClelland, J.W., Peterson, B.J., Shiklomanov, I.A., Shiklomanov, A.I., Zhulidov, A.V., Gordeev, V.V., Bobrovitskaya, N.N., 2002. A circumpolar perspective on fluvial sediment flux to the Arctic ocean. Global Biogeochem. Cycles 16. https://doi.org/10.1029/2001GB001849, 45-1-45–14.

Jafar-Sidik, M., Gohin, F., Bowers, D., Howarth, J., Hull, T., 2017. The relationship between suspended particulate matter and turbidity at a mooring station in a coastal environment: consequences for satellite-derived products. Oceanologia 59, 365–378. https://doi.org/10.1016/j.oceano.2017.04.003.

Jain, S.K., Singh, V.P., 2003. Emerging techniques for data acquisition and systems modeling. In: Jain, S.K., Singh, V.P. (Eds.), Developments in Water Science. Elsevier, Amsterdam, The Netherlands, pp. 123–205. https://doi.org/10.1016/S0167-5648(03)80057-6.

Jones, B.M., Arp, C.D., Jorgenson, M.T., Hinkel, K.M., Schmutz, J.A., Flint, P.L., 2009. Increase in the rate and uniformity of coastline erosion in Arctic Alaska. Geophys. Res. Lett. 36, 1–5. https://doi.org/10.1029/2008GL036205.

Jong, D., Bröder, L., Tanski, G., Fritz, M., Lantuit, H., Tesi, T., Haghipour, N., Eglinton, T. I., Vonk, J.E., 2020. Nearshore zone dynamics determine pathway of organic carbon from eroding permafrost coasts. Geophys. Res. Lett. 47 https://doi.org/10.1029/2020GL088561.

Klein, K.P., Lantuit, H., Heim, B., Fell, F., Doxaran, D., Irrgang, A.M., 2019. Long-term high-resolution sediment and sea surface temperature spatial patterns in Arctic nearshore waters retrieved using 30-year Landsat archive imagery. Rem. Sens. 11 (23), 2791. https://doi.org/10.3390/rs11232791.

Knaeps, E., Ruddick, K.G., Doxaran, D., Dogliotti, A.I., Nechad, B., Raymaekers, D., Sterckx, S., 2015. A SWIR based algorithm to retrieve total suspended matter in extremely turbid waters. Remote Sens. Environ. 168, 66–79. https://doi.org/10.1016/j.rse.2015.06.022.

Lantuit, H., Overduin, P.P., Wetterich, S., 2013. Recent progress regarding permafrost coasts. Permafr. Periglac. Process. 24, 120–130. https://doi.org/10.1002/ppp.1777.

Lantuit, H., Pollard, W.H., 2008. Fifty years of coastal erosion and retrogressive thaw slump activity on Herschel Island, southern Beaufort Sea, Yukon Territory, Canada. Geomorphology 95, 84–102. https://doi.org/10.1016/j.geomorph.2006.07.040.

Lim, M., Whalen, D., Mann, J., Fraser, P., Berry, H.B., Irish, C., Cockney, K., Woodward, J., 2020. Effective monitoring of permafrost coast erosion: wide-scale storm impacts on outer islands in the Mackenzie delta area. Front. Earth Sci. 8, 1–17. https://doi.org/10.3389/feart.2020.561322.

Mackay, J.R., 1971. The origin of Massive Icy Beds in Permafrost, Western Arctic Coast, Canada. Can. J. Earth Sci. 8, 397–422.

Manzo, C., Braga, F., Zaggia, L., Brando, V.E., Giardino, C., Bresciani, M., Bassani, C., 2018. Spatio-temporal analysis of prodelta dynamics by means of new satellite generation: the case of Po river by Landsat-8 data. Int. J. Appl. Earth Obs. Geoinf. 66, 210–225. https://doi.org/10.1016/j.jag.2017.11.012.

McClelland, J.W., Déry, S.J., Peterson, B.J., Holmes, R.M., Wood, E.F., 2006. A pan-arctic evaluation of changes in river discharge during the latter half of the 20th century. Geophys. Res. Lett. 33, 2–5. https://doi.org/10.1029/2006GL025753.

McClelland, J.W., Holmes, R.M., Peterson, B.J., Raymond, P.A., Striegl, R.G., Zhulidov, A.V., Zimov, S.A., Zimov, N., Tank, S.E., Spencer, R.G.M., Staples, R., Gurtovays, T.Y., Griffin, C.G., 2016. Particulate organic carbon and nitrogen export from major Arctic rivers. Global Biogeochem. Cycles 30, 629–643. https://doi.org/10.1111/1462-2920.13280.

McGillivray, D.G., Agnew, T.A., McKay, G.A., Pilkington, G.R., Hill, M.C., 1993. Impacts of climatic change on the Beaufort sea-ice regime: implications for the Arctic petroleum industry. In: Climate Change Digest CCD, vols. 93–01. Environment Canada, Atmospheric Environment Service, Downsview - Ontario.

Mobley, C.D., 1999. Estimation of the remote-sensing reflectance from above-surface measurements. Appl. Opt. 38 https://doi.org/10.1364/AO.38.007442.

Munday, J.C., Alföldi, T.T., 1979. LANDSAT test of diffuse reflectance models for aquatic suspended solids measurement. Remote Sens. Environ. 8, 169–183. https://doi.org/10.1016/0034-4257(79)90015-4.

Nechad, B., Dogliotti, A.I., Ruddick, K.G., Doxaran, D., 2016. Particulate backscattering and suspended matter concentration retrieval from remote-sensed turbidity in various coastal and riverine turbid waters. In: Ouwehand, L. (Ed.), Proceedings of ESA Living Planet Symposium, SP 740. ESA Communications, Prague, p. 13, 9,5.

Nechad, B., Ruddick, K.G., Neukermans, G., 2009. Calibration and validation of a generic multisensor algorithm for mapping of turbidity in coastal waters. In: Bostater, C.R.J., Mertikas, S.P., Neyt, X., Velez-Reyes, M. (Eds.), Proceedings of SPIE - the International Society for Optical Engineering, vol. 7473, pp. 1–11. https://doi.org/10.1117/12.830700, 7473H.

Neukermans, G., Loisel, H., Me, X., Astoreca, R., Mckee, D., 2012. In situ variability of mass-specific beam attenuation and backscattering of marine particles with respect to particle size , density , and composition. Limnol. Oceanogr. 57, 124–144. https://doi.org/10.4319/lo.2011.57.1.0124.

Nielsen, D.M., Dobrynin, M., Baehr, J., Razumov, S., Grigoriev, M., 2020. Coastal erosion variability at the southern Laptev Sea linked to winter sea ice and the Arctic oscillation. Geophys. Res. Lett. 47, 1–11. https://doi.org/10.1029/2019GL086876.

Nowak, A., Hodgkins, R., Nikulina, A., Osuch, M., Wawrzyniak, T., Kavan, J., Majerska, M., Romashova, K., Vasilevich, I., Sobota, I., Rachlewicz, G., Kingdom, U., Republic, C., Management, S., 2019. From Land to Fjords: the Review of Svalbard Hydrology from 1970 to 2019 (SvalHydro). SESS Report 2020, pp. 176–201. https://doi.org/10.5281/zenodo.4294063 176. Svalbard Integrated Arctic Earth Observing System. Longyearbyen, Svalbard.

O'Brien, M.C., Macdonald, R.W., Melling, H., Iseki, K., 2006. Particle fluxes and geochemistry on the Canadian Beaufort Shelf: implications for sediment transport and deposition. Continent. Shelf Res. 26, 41–81. https://doi.org/10.1016/j.csr.2005.09.007.

Obu, J., Lantuit, H., Fritz, M., Pollard, W.H., Sachs, T., Günther, F., 2016. Relation between planimetric and volumetric measurements of permafrost coast erosion: a case study from Herschel Island, western Canadian Arctic. Polar Res. 35, 1–13. https://doi.org/10.3402/polar.v35.30313.

Pahlevan, N., Mangin, A., Balasubramanian, S.V., Smith, B., Alikas, K., Arai, K., Barbosa, C., Bélanger, S., Binding, C., Bresciani, M., Giardino, C., Gurlin, D., Fan, Y., Harmel, T., Hunter, P., Ishikaza, J., Kratzer, S., Lehmann, M.K., Ligi, M., Ma, R., Martin-Lauzer, F.R., Olmanson, L., Oppelt, N., Pan, Y., Peters, S., Reynaud, N., Sander de Carvalho, L.A., Simis, S., Spyrakos, E., Steinmetz, F., Stelzer, K., Sterckx, S., Tormos, T., Tyler, A., Vanhellemont, Q., Warren, M., 2021. ACIX-Aqua: a global assessment of atmospheric correction methods for Landsat-8 and Sentinel-2 over lakes, rivers, and coastal waters. Remote Sens. Environ. 258 https://doi.org/10.1016/j.rse.2021.112366.

Radosavljevic, B., Lantuit, H., Pollard, W., Overduin, P., Couture, N., Sachs, T., Helm, V., Fritz, M., 2015. Erosion and flooding—threats to coastal infrastructure in the Arctic: a case study from Herschel Island, Yukon Territory, Canada. Estuar. Coast 39, 900–915. https://doi.org/10.1007/s12237-015-0046-0.

Renosh, P.R., Doxaran, D., De Keukelaere, L., Gossn, J.I., 2020. Evaluation of atmospheric correction algorithms for sentinel-2-MSI and sentinel-3-OLCI in highly turbid estuarine waters. Rem. Sens. 12 https://doi.org/10.3390/RS12081285.

Rolph, R., Overduin, P.P., Ravens, T., Lantuit, H., Langer, M., 2021. ArcticBeach v1.0: a physics-based parameterization of pan-Arctic coastline erosion. Geosci. Model Dev. Discuss. (GMDD) 1–26. https://doi.org/10.5194/gmd-2021-28.

Romanovsky, V.E., Smith, S.L., Christiansen, H.H., 2010. Permafrost thermal state in the polar northern hemisphere during the international polar year 2007-2009: a synthesis. Permafr. Periglac. Process. 21, 106–116. https://doi.org/10.1002/ppp.689.

Ruddick, K.G., Cauwer, V. De, Park, Y., Moore, G., 2006. Seaborne measurements of near infrared water-leaving reflectance: the similarity spectrum for turbid waters. Limnol. Oceanogr. 51, 1167–1179. https://doi.org/10.4319/lo.2006.51.2.1167.

Sent, G., Vieira de Sa, C., Dogliotti, A.I., 2020. Remote Sensing for Water Quality Studies : Test of Suspended Particulate Matter and Turbidity Algorithms for Portuguese Transitional and Inland Waters. PhD-Thesis. submitted at the. University of Lisbon.

Serreze, M.C., Barry, R.G., 2011. Processes and impacts of Arctic amplification: a research synthesis. Global Planet. Change 77, 85–96. https://doi.org/10.1016/j.gloplacha.2011.03.004.

Solomon, S.M., 2005. Spatial and temporal variability of shoreline change in the Beaufort-Mackenzie region, northwest territories, Canada. Geo Mar. Lett. 25, 127–137. https://doi.org/10.1007/s00367-004-0194-x.

Tang, S., Larouche, P., Niemi, A., Michel, C., 2013. Regional algorithms for remote-sensing estimates of total suspended matter in the Beaufort Sea. Int. J. Rem. Sens. 34, 6562–6576. https://doi.org/10.1080/01431161.2013.804222.

Tank, S.E., Fellman, J.B., Hood, E., Kritzberg, E.S., 2018. Beyond respiration: controls on lateral carbon fluxes across the terrestrial-aquatic interface. Limnol. Oceanogr. Lett. 3, 76–88. https://doi.org/10.1002/lol2.10065.

Tanski, G., Bröder, L., Wagner, D., Knoblauch, C., Lantuit, H., Beer, C., Sachs, T., Fritz, M., Tesi, T., Koch, B.P., Haghipour, N., Eglinton, T.I., Strauss, J., Vonk, J.E., 2021. Permafrost Carbon and CO2 pathways differ at contrasting coastal erosion sites in the Canadian Arctic. Front. Earth Sci. 9, 1–20. https://doi.org/10.3389/feart.2021.630493.

Tanski, G., Lantuit, H., Ruttor, S., Knoblauch, C., Radosavljevic, B., Strauss, J., Wolter, J., Irrgang, A.M., Ramage, J., Fritz, M., 2017. Transformation of terrestrial organic matter along thermokarst-affected permafrost coasts in the Arctic. Sci. Total Environ. 581–582, 434–447. https://doi.org/10.1016/j.scitotenv.2016.12.152.

Tanski, G., Wagner, D., Knoblauch, C., Fritz, M., Sachs, T., Lantuit, H., 2019. Rapid CO 2 release from eroding permafrost in seawater. Geophys. Res. Lett. 46 https://doi.org/10.1029/2019GL084303.

Terhaar, J., Lauerwald, R., Regnier, P., Gruber, N., Bopp, L., 2021. Around one third of current Arctic Ocean primary production sustained by rivers and coastal erosion. Nat. Commun. 12, 1–10. https://doi.org/10.1038/s41467-020-20470-z.

Vanhellemont, Q., 2019. Remote sensing of environment adaptation of the dark spectrum fitting atmospheric correction for aquatic applications of the Landsat and Sentinel-2 archives. Remote Sens. Environ. 225, 175–192. https://doi.org/10.1016/j.rse.2019.03.010.

Vanhellemont, Q., Ruddick, K., 2021. Atmospheric correction of Sentinel-3/OLCI data for mapping of suspended particulate matter and chlorophyll-a concentration in Belgian turbid coastal waters. Remote Sens. Environ. 256, 112284. https://doi.org/10.1016/j.rse.2021.112284.

Vanhellemont, Q., Ruddick, K., 2018. Atmospheric correction of metre-scale optical satellite data for inland and coastal water applications. Remote Sens. Environ. 216, 586–597. https://doi.org/10.1016/j.rse.2018.07.015.

Vanhellemont, Q., Ruddick, K., 2014. Turbid wakes associated with offshore wind turbines observed with Landsat 8. Remote Sens. Environ. 145, 105–115. https://doi.org/10.1016/j.rse.2014.01.009.

Vonk, J.E., Sánchez-García, L., van Dongen, B.E., Alling, V., Kosmach, D., Charkin, A., Semiletov, I.P., Dudarev, O.V., Shakhova, N., Roos, P., Eglinton, T.I., Andersson, A., Gustafsson, Ö., 2012. Activation of old carbon by erosion of coastal and subsea permafrost in Arctic Siberia. Nature 489, 137–140. https://doi.org/10.1038/nature11392.

Walch, D.M.R., 2021. Spatio-temporal Variability in Suspended Particulate Matter in a High Arctic Estuary (Adventfjorden , Svalbard): A Combined Field- and Remote Sensing Approach. MSc-Thesis, submitted at the University of Potsdam.

Weege, S., 2016. Climatic Drivers of Retrogressive Thaw Slump Activity and Resulting Sediment and Carbon Release to the Nearshore Zone of Herschel Island, Yukon Territory, Canada. PhD-Thesis. submitted at the. University of Potsdam.

Wegner, C., Bennett, K.E., de Vernal, A., Forwick, M., Fritz, M., Heikkilä, M., Łącka, M., Lantuit, H., Laska, M., Moskalik, M., O'Regan, M., Pawłowska, J., Promińska, A., Rachold, V., Vonk, J.E., Werner, K., 2015. Variability in transport of terrigenous material on the shelves and the deep Arctic Ocean during the Holocene. Polar Res. 34, 24964. https://doi.org/10.3402/polar.v34.24964.

Węsławski, J.M., Gluchowska, M., Szczucinski, W., Tatarek, A., Wiktor, J., Wlodarska-Kowalczuk, M., Zajaczkowski, M., 2011. In: Węsławski, J.M. (Ed.), Adventfjorden: Arctic Sea in the Backyard, first ed. Institute of Oceanology Polish Academy of Sciences, Sopot, Poland.

Williams, W.J., Carmack, E.C., Shimada, K., Melling, H., Aagaard, K., Macdonald, R.W., Grant Ingram, R., 2006. Joint effects of wind and ice motion in forcing upwelling in Mackenzie Trough, Beaufort Sea. Continent. Shelf Res. 26, 2352–2366. https://doi.org/10.1016/j.csr.2006.06.012.

World Glacier Monitoring Service, 2020. World Glacier Monitoring Database. https://doi.org/10.5904/wgms-fog-2020-08. Zurich, Switzerland.

Xue, C., Zhang, T., Chen, S., Wu, X., Yan, F., 2019. A novel estimation method for SPM in China eastern coastal waters based on conventional hydrological profile measurements. Estuar. Coast Shelf Sci. 230, 106444. https://doi.org/10.1016/j.ecss.2019.106444.

Yang, D., Shi, X., Marsh, P., 2015. Variability and extreme of Mackenzie River daily discharge during 1973-2011. Quat. Int. 380–381, 159–168. https://doi.org/10.1016/j.quaint.2014.09.023.

Zajaczkowski, M., Włodarska-Kowalczuk, M., 2007. Dynamic sedimentary environments of an Arctic glacier-fed river estuary (Adventfjorden, Svalbard). I. Flux, deposition, and sediment dynamics. Estuar. Coast Shelf Sci. 74, 285–296. https://doi.org/10.1016/j.ecss.2007.04.015.